Carbon 142 (2019) 291–299

Contents lists available at ScienceDirect

Carbon

journal homepage: www.elsevier.com/locate/carbon

# High temperature quasistatic and dynamic mechanical behavior of interconnected 3D carbon nanotube structures

Sanjit Bhowmick [a, *, 1], Sehmus Ozden [b, 1], Rafael A. Bizão [d], Leonardo Dantas Machado [e], S.A. Syed Asif [a], Nicola M. Pugno [d, f, g], Douglas S. Galvão [h, **], Chandra Sekhar Tiwary [c, i, ***], P.M. Ajayan [c, ****]

[a] Bruker Nano Surfaces, Minneapolis, MN 55344, USA
[b] Materials Physics and Applications Division, Los Alamos National Laboratory, Los Alamos NM 87545, USA
[c] Materials Science and Nanoengineering, Rice University, Houston, TX, 77005, USA
[d] Department of Civil, Environmental and Mechanical Engineering, Laboratory of Bio-Inspired and Graphene Nanomechanics, University of Trento, via Mesiano, 77, 38123 Trento, Italy
[e] Departamento de Física Teórica e Experimental, Universidade Federal do Rio Grande do Norte, Natal, RN, 59072-970, Brazil
[f] Ket-Lab, Edoardo Amaldi Foundation, Italian Space Agency, Via del Politecnico snc, 00133 Rome, Italy
[g] School of Engineering and Materials Science, Queen Mary University of London, Mile End Road, London E1 4NS, United Kingdom
[h] Applied Physics Department, State University of Campinas, Campinas, SP, 13083-959, Brazil
[i] Metallurgical and Materials Engineering, Indian Institute of Technology, Kharagpur, WB, 721302, India

ARTICLE INFO

*Article history:*
Received 28 May 2018
Received in revised form
3 September 2018
Accepted 26 September 2018
Available online 8 October 2018

*Keywords:*
Carbon nanotubes
In-situ nanomechanics
High temperature testing
Fatigue testing
MD simulation

ABSTRACT

Carbon nanotubes (CNTs) are one of the most appealing materials in recent history for both research and commercial interest because of their outstanding physical, chemical, and electrical properties. This is particularly true for 3D arrangements of CNTs which enable their use in larger scale devices and structures. In this paper, the effect of temperature on the quasistatic and dynamic deformation behavior of 3D CNT structures is presented for the first time. An *in situ* high-temperature nanomechanical instrument was used inside an SEM at high vacuum to investigate mechanical properties of covalently interconnected CNT porous structures in a wide range of temperature. An irreversible bucking at the base of pillar samples was found as a major mode of deformation at room and elevated temperatures. It has been observed that elastic modulus and critical load to first buckle formation decrease progressively with increasing temperature from 25 °C to 750 °C. To understand fatigue resistance, pillars made from this unique structure were compressed to 100 cycles at room temperature and 750 °C. While the structure showed remarkable resistance to fatigue at room temperature, high temperature significantly lowers fatigue resistance. Molecular dynamics (MD) simulation of compression highlights the critical role played by covalent interconnections which prevent localized bending and improve mechanical properties.



## 1. Introduction

Carbon nanotubes (CNTs), extraordinary materials with exceptional mechanical, chemical, electrical, thermal, and functional properties, have attracted the attention of scientists from different fields [1,2]. In the past two decades, CNTs have been explored for different applications, ranging from energy storage to high impact resistance materials [3–5]. Their low density and high-temperature stability along with ~1 TPa elastic modulus of individual nanowires have been a drive for a broad range of structural applications [3,6,7]. For more than a decade, three-dimensional (3D) CNT-based architectures have been synthesized and their mechanical properties have been tested under different loading and strain conditions [8–11]. Such 3D structures show unique mechanical behavior such as superelasticity, viscoelasticity, self-

* Corresponding author.
** Corresponding author.
*** Corresponding author. Materials Science and Nanoengineering, Rice University, Houston, TX, 77005, USA.
**** Corresponding author.
*E-mail addresses:* Sanjit.Bhowmick@bruker.com (S. Bhowmick), galvao@ifi.unicamp.br (D.S. Galvão), cst.iisc@gmail.com (C.S. Tiwary), ajayan@rice.edu (P.M. Ajayan).
[1] S. B. and S. O. contributed equally to this work.

https://doi.org/10.1016/j.carbon.2018.09.075
0008-6223/

stiffening, high-frequency damping, and others [12–16]. Undoubtedly, most of these properties are important for specific structural applications and are not observed in conventional bulk ceramics and metals. In some applications, mechanical behavior at elevated temperatures is one of the key issues as the engineering components are exposed to high-temperature environment [17,18]. Evaluation of high-temperature properties of CNT based architectures has remained unexplored so far, in part due to experimental difficulties. Although CNTs start oxidizing above 500 °C in the ambient environment, they are stable at higher temperature in vacuum and inert atmosphere. Thus, an inert or vacuum environment is essential for evaluation of its high-temperature mechanical properties. To understand mechanical behavior of small-scale CNT structures, we also need high precision instruments that can operate at an elevated temperature in vacuum. In this study, nanomechanical instrument was used to conduct high temperature mechanical testing at a vacuum level of ~$10^{-6}$ Torr and at a maximum temperature of 750 °C.

We have chosen CVD grown vertically aligned interconnected nanotubes (reported to be the nanotube 3D architecture with highest stiff) for our mechanical testing [19,20]. To maintain uniform samples for testing, square cross-section of micro-pillars were fabricated from the 3D carpet of CNTs. High-resolution SEM was used for capturing video and images during testing and to correlate mechanical properties with deformation behavior. To gain further insights into the deformation process, fully atomistic reactive molecular dynamics simulations were carried out.

Supplementary video related to this article can be found at https://doi.org/10.1016/j.carbon.2018.09.075.

### 1.1. Experimental procedure

#### 1.1.1. CNT growth

The blocks of carbon nanotubes were grown by chemical vapor deposition using ferrocene and xylene on silicon wafer substrates. Detail of the synthesizing technique of 3D structure is discussed elsewhere [7,19]. The surface of the substrate was sputtered by 10 nm aluminum and 1.5 nm iron films prior to the growth process. This technique allowed to produce the interconnected 3D-CNT scaffold in varying sizes. The density of 3D structure can be varied 0.13–0.32 mg/mm [3,19]. The morphology and structural properties of interconnected CNTs were investigated by scanning electron microscopy (Quanta ESEM, FEI Company) and transmission electron microscopy, 2100F (JEOL), Raman microscopy, 633 nm laser (Renishaw), and X-ray photoelectron spectroscopy.

#### 1.1.2. Sample preparation and high temperature mechanical testing

An *in situ* nanomechanical instrument, PI 88 SEM PicoIndenter (Bruker Nano Surfaces) with an integrated high-temperature stage and an active tip heating, Fig. 1a, was used to conduct uniaxial compression of pillar samples. Micropillars of dimensions 15 μm × 15 μm in cross-section and 25–30 μm in height were prepared from the middle of the bulk sample by focused ion beam (FIB) as shown in Fig. 1b–c. The quasistatic and dynamic compression tests were conducted with a 20 μm flat punch diamond probe. Using the displacement-controlled feedback mode of the system, the pillars were compressed to 8–38% strain at a strain rate of $10^{-3}$ $s^{-1}$. The tests were conducted at room temperature (RT) as well as at several elevated temperatures of up to 750 °C. *In situ* mechanical testing allowed precise alignment of the tip with the sample as well as direct and real-time observation of the deformation processes. A benefit of performing these tests in the SEM is that the high vacuum environment limits oxidation and degradation of the sample, especially at high temperatures. Water circulation through cooling blocks at the sample heater and transducer minimizes thermal drift of the system.

#### 1.1.3. Simulation details

Molecular dynamics simulations (MD) were carried out using the Mueller parametrization [21] of the Reactive Force Field (ReaxFF) [22], as implemented in the LAMMPS MD package [23]. The model CNT pillars were comprised of 5 × 5 arrays of 10 nm long double-walled carbon nanotubes (DWNT). Structures with and without interconnections were considered for the simulation. For the former, we used defective (5% vacancies) (5,10) CNTs inside (10,10) CNTs. For the latter, we considered pristine (5,5) CNTs inside (10,10) CNTs. Before carrying out compression tests, we first minimized and then thermalized our model systems for 400000 steps in the NVT ensemble, using a chain of three Nosé-Hoover thermostats. A time-step of 0.1 fs was employed during all simulations. For the constant force compression tests, the bottom side of the pillar was fixed, and the top side was treated as a rigid body keeping the external torque components null in order to avoid undesired rotations. At this point, a force of $F = 2584$ nN was applied to the top side of the pillar, equally distributed between all its constituent atoms. We considered two temperatures within the range of the experimental setup: 27 °C and 727 °C. For the constant indenter velocity tests, a planar surface was displaced downwards at a constant rate of 0.5 Å/ps while the bottom part of the CNT pillar was kept fixed.

## 2. Results and discussion

Interconnected CNTs were grown by CVD method on a silica substrate, as described in detail in our previous publication [19]. The mechanism of formation of these interconnected 3D structures is explained as following: the initial CNT grows on the catalyst deposited substrate, similar to regular CNT forest that grown using CVD methods [7]. However, after the initial growth of a CNTs started, the secondary catalyst (i.e. carbon source and iron) deposit on the growing CNT and acts as a nucleation site for the growth of another CNT as a branch. To understand the morphology of the interconnected CNTs, the top and side surface of as grown interconnected CNT blocks was imaged by SEM (Fig. 1c–e). CNT blocks have uniform microstructure and evenly distributed microporosites. The side view of SEM images shows that CNT pillars consist of interconnected network structures (Fig. 1e–g). The bright-field TEM images (Fig. 1h–k) confirm that individual nanotube structures are interconnected and covalently bonded. Fig. 1 shows the Raman spectra of interconnected CNTs, which consist of two main peaks, G-band (at 1585 $cm^{-1}$) and D-band (at 1343 $cm^{-1}$), associated with graphitic-like and disordered structures, respectively [24]. A quantitative measurement of the defect density in the CNT sidewall can be determined by the ratio of these two bands, $I_D$: $I_G$ (0.58), which is related to the number of defects on the surface of nanotubes and at the junctions between individual CNTs. In addition, the full-width-half-maximum (FWHM) of D-band is also related to the quality of CNTs. In general, when the quality of the CNTs samples increases, the FWHM of D-band decreases. Here, the FWHM of D-band and G-band is 165.5 and 67.9 respectively. The high FWHM of the D-band is due to the defects on the surface of CNTs and between individual junctions. The peak at ~2700 $cm^{-1}$ indicate the G′-band, which is the second order of the D band and is referred to as its overtone. The 2D-band originated from a two-phonon lattice vibrational process, but unlike the D-band, it is not related to defects of the nanotubes. XPS was used for quantitative chemical analysis of interconnected nanotubes (Fig. 1m). The C1s core level peak positions of the carbon and oxygen atoms are approximately at 285 eV and 532 eV respectively

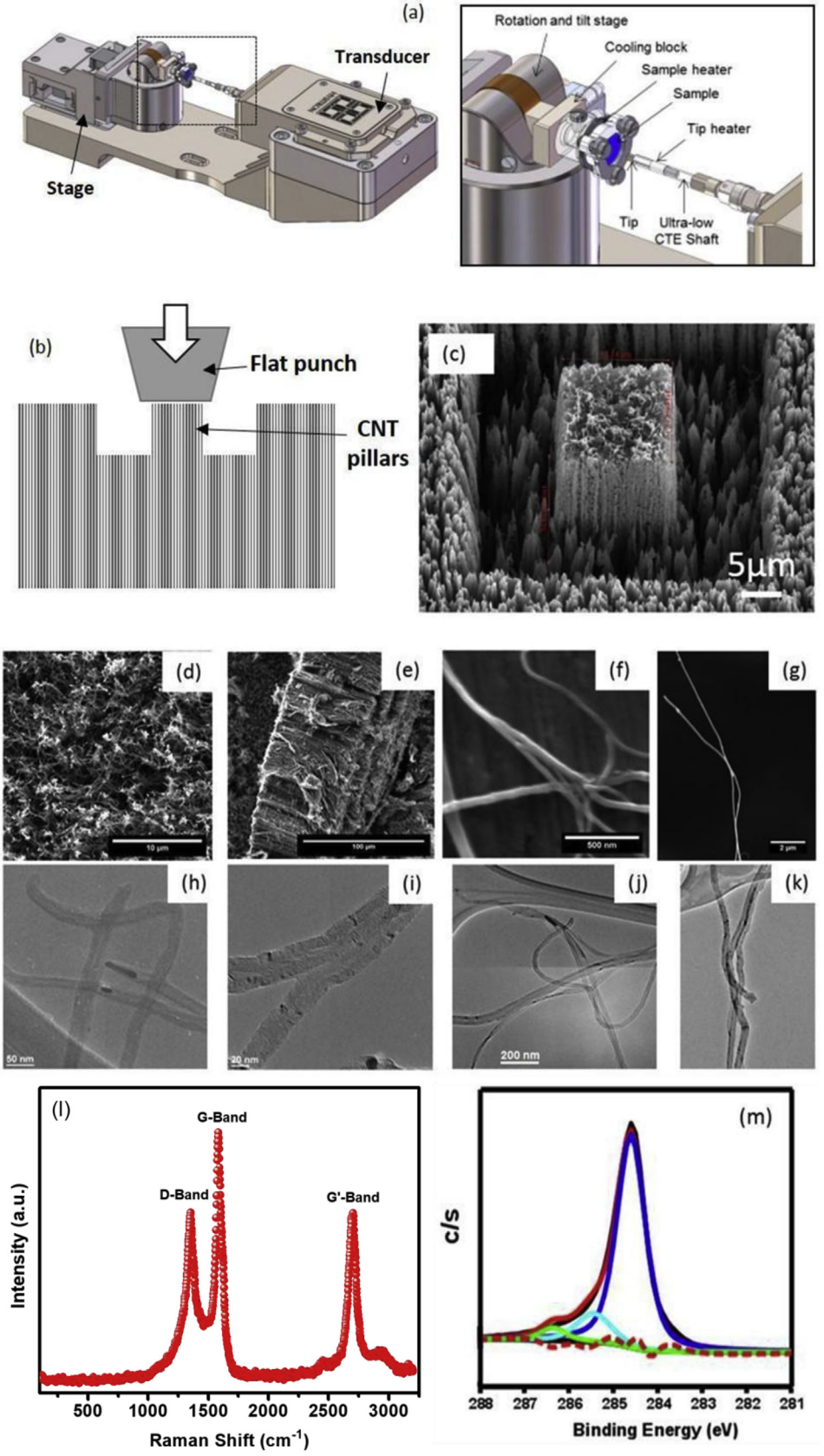


**Fig. 1.** (a) Schematic view of *in situ* SEM nanomechanical instrument showing different components of high temperature system, (b) Schematic depicting the geometry of the sample used for pillar compression, (c) Tilted SEM image of the pillar sample prepared by focused ion beam, (d) Low magnification top view and (e) side view of the 3D interconnected carbon nanotube architecture, (f)–(g) High magnification SEM image of interconnected nanotubes, (h)–(k) Bright field TEM images of the nanotubes showing the junctions, (l) Raman spectrum (m) XPS of the interconnected nanotubes. (A colour version of this figure can be viewed online.)

(Fig. S1). The peak position at 284.5 eV, 285.4 eV and 286.2 eV corresponds to C-C, C-O and C=O bonds respectively.

Fig. 2a displays a typical engineering stress - engineering strain plot which is calculated from load-displacement data obtained from a displacement-controlled test conducted at room temperature. The plot shows that stress increases linearly with strain until a critical stress at point A ($\sigma_A$), at which stress dropped to a lower stress plateau, called instability stress at point B ($\sigma_B$). As the strain on the structure increases (B-C), several small stress drops can be observed. Fig. 2b–d shows microstructural changes at the pillar base. Microstructural images in this study and others [15,25] confirm that the critical stress ($\sigma_A$) is associated with the formation of the first buckling wrinkle at the bottom of the pillars (Fig. 2b). As strain increases, additional wrinkles are formed which lead to small stress drops in the stress-strain plots (B-C). The overall changes in the microstructure indicate a collective buckling behavior, as illustrated in Fig. 2c [26]. Under an applied load, the CNT sections of turfs, which has a fully constrained base, reorient towards one direction to accommodate the plastic strain. The local position at where the buckling starts depends on the density and the microstructure of the scaffolds. In our post-mortem analysis, the maximum density of buckle formation was observed near the base,

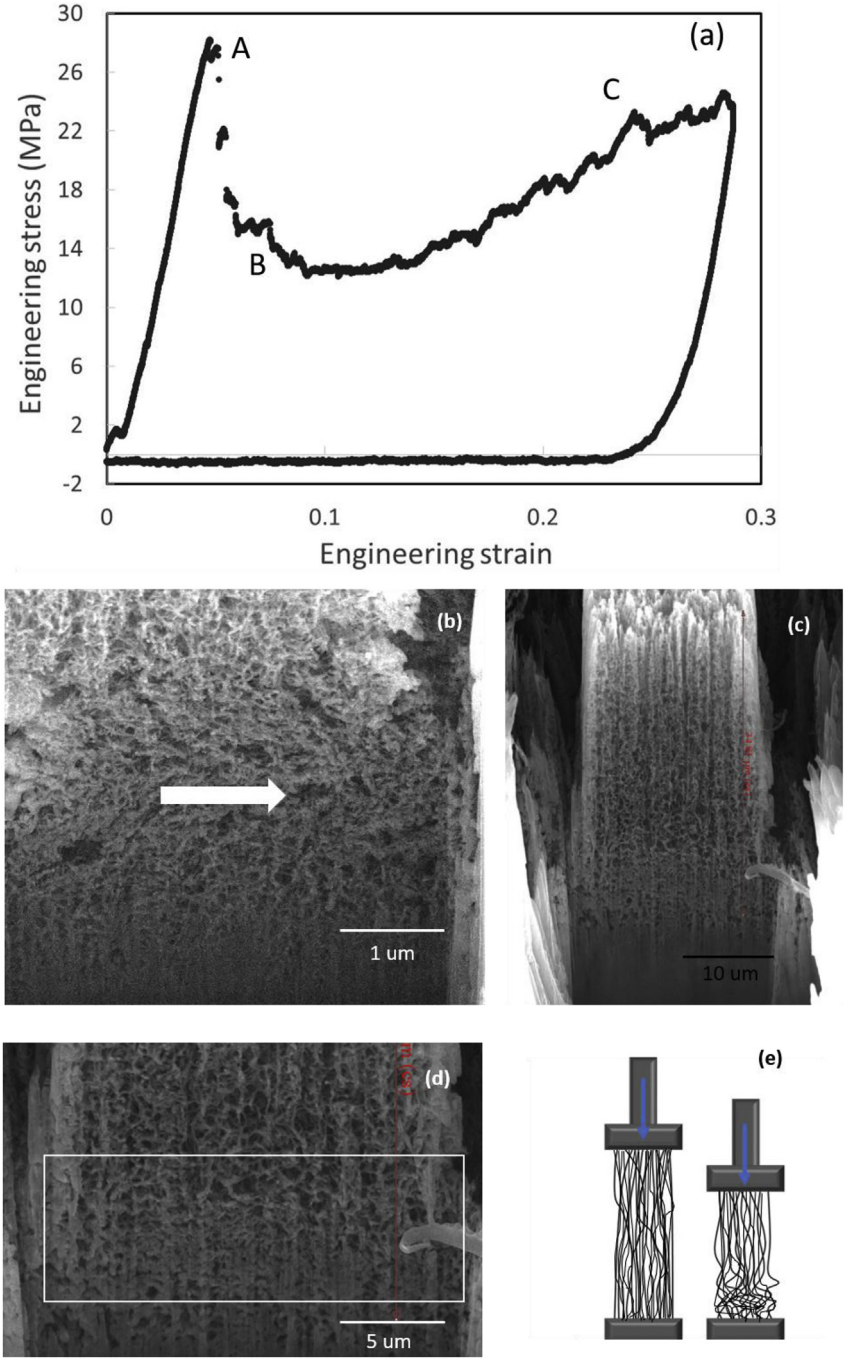


**Fig. 2.** (a) A typical engineering stress vs engineering strain curve at room temperature. (b) High magnification SEM image of the base of the pillar showing buckling of the nanotubes marked by an arrow. (c)–(d) SEM images of the pillar showing high density region at the base of the pillar. (e) Schematic showing the primary mode of deformation which is a buckling event at the base of the pillar. (A colour version of this figure can be viewed online.)

which is shown in a high-magnification image in Fig. 2d.

Next, the results from high-temperature mechanical tests are discussed. Stress-strain plots of pillar compression at room temperature to 750 °C are shown in Fig. 3a. The pillars were compressed to a range of strain from 8% to 38%. It can be noticed that the pattern of stress-strain curves remains the same at all the temperatures although $\sigma_A$ decreases with increasing temperature. This indicates that temperature has an influence on the nucleation of buckling event in the nanotubes. The change in slope in the linear part of the stress-strain plots indicates that elastic modulus decreases with increase in temperature, which is plotted in Fig. 3b. An average elastic modulus was calculated to be 640 MPa at RT, which

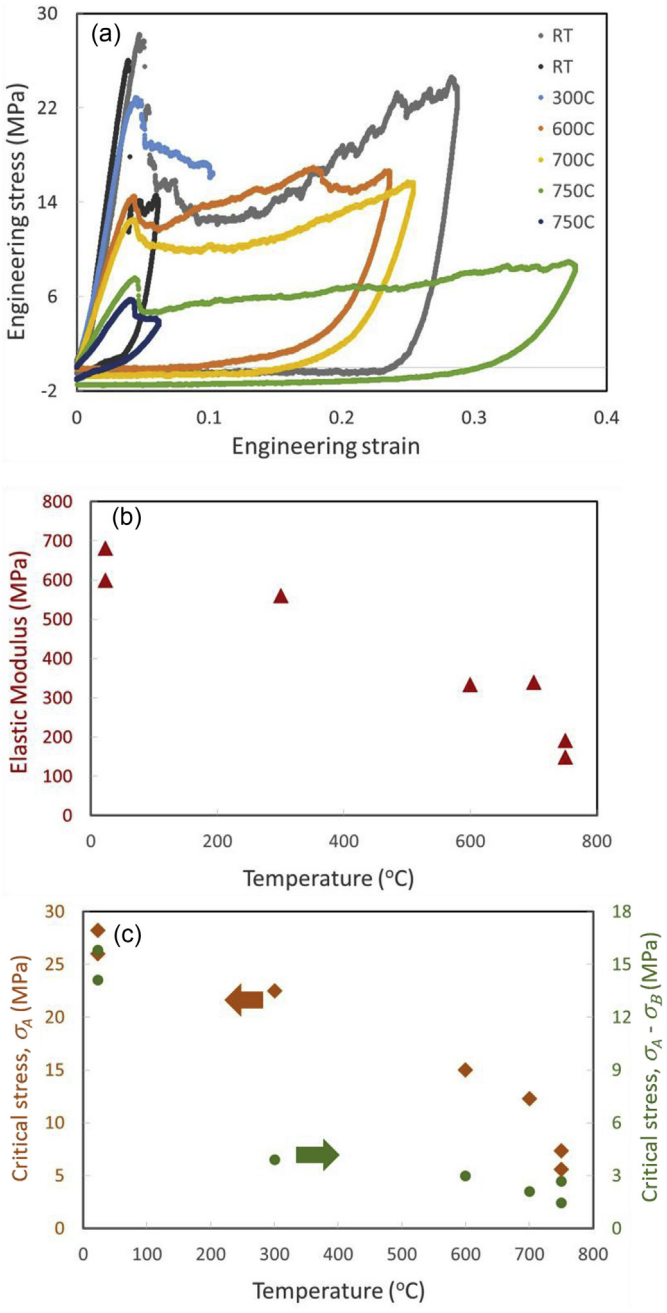


**Fig. 3.** (a) Engineering stress vs engineering strain of the interconnected 3D CNTs at different temperatures (RT, 300, 600, 700 and 750 °C). (b) Variation in Elastic modulus with temperature, (c) Change in critical stress ($\sigma_A$) and stress drop drop ($\sigma_A$ - $\sigma_B$) as a function of temperature. (A colour version of this figure can be viewed online.)

decreases to 530 MPa at 300 °C (7% change), to 300 MPa at 600-700 °C (46% change) and 150 MPa at 750 °C (70%). Critical stress for first buckle formation, $\sigma_A$ and net stress drop, $\sigma_A$ - $\sigma_B$, are plotted as a function of temperature in Fig. 3c $\sigma_A$ changes more linearly with temperature; $\sigma_A$ at RT was found to be 27.2 MPa which reduces by 77% at 750 °C. On the other hand, a sharp decrease in stress-drop ($\sigma_A$ - $\sigma_B$) can be observed only at 300 °C and then net stress does not change significantly with temperature. The results confirm that temperature has a significant influence to initiate a bucking event in the 3D structure. At higher temperature, lattice fluctuations promote lowering of bond strength at the interfaces of CNTs resulting an easy buckling event. It has been reported that heating at inert atmosphere at elevated temperature causes progressive destruction of the integrity of CNT structure [27,28].

Analytical calculations were developed in order to describe the strong dependence of the elastic modulus with the temperature. Our calculations were based in a model [29] that describes a parallel array of nanotubes under compression with a simple modification that adds a temperature dependence and a global contribution to it, in a way that the effective elastic modulus ($E'$) is calculated as

$$E' = \frac{E_0\varphi}{1 + tan^2(\theta)\lambda'^2/3}\left(1 - \frac{T}{T^*}\right)^{\alpha}, \quad (1)$$

in which $E_0$ is the intrinsic CNT elastic modulus at $T = 0$, $\varphi$ is the nominal density factor, $\theta$ is the average inclination angle, $T^*$ and $\alpha$ are critical parameters to be determined and $\lambda' = \lambda_l(1 - i) + i\lambda_g$ depends on the individual contributions of the local ($\lambda_l$) and global slenderness ($\lambda_g$) according to the interaction factor ($i$). Adding the same global contribution to the plateau strength $\sigma_p$ (here considered as the average between $\sigma_A$ and $\sigma_B$) we get

$$\sigma_p = \frac{\pi\left(1 + tan^2(\theta)\lambda'^2/3\right)}{4\lambda'^2}E'. \quad (2)$$

Considering that the 3D CNT structures have a square base of side $l \approx 15\ \mu$m filled with perfect cylinders of length $L \approx 27.5\mu$m and radius $r \approx 15$nm we can calculate the local and global slenderness as $\lambda_l = 2L/r \approx 3667$ and $\lambda_g = L\sqrt{12}/l \approx 6.35$, respectively. The 3D CNT structures density $d_e \approx 0.225$ g/cm$^3$ and the theoretical density for multi-walled CNTs $d_t \approx 2.45$g/cm$^3$ [30] lead us to a nominal density fraction $\varphi = d_e/d_t \approx 0.092$, which means that the experimental structure has ~91% of free space when compared to the theoretical one.

Based on the above equations and considering $E_0 = 1$TPa, it is possible to derive the coefficients by doing a best fit together with the experimental data. This lead us to $T^* \approx 1100$K, $\alpha \approx 0.49$, $\theta \approx 19°$ and $i \approx 0.99$ with a good fit of the data (see Fig. 6). It is possible to conclude that the 3D CNT structures have a strong dependence on the temperature characterized by a drastic drop on its elastic properties and if experiments at higher temperatures are considered this effect is expected to be even stronger and the mechanical properties more affected. The 3D CNT structures could also have a small inclination and the global slenderness has a very significant role in the compression process. Also, Eq. (1) together with the parameters obtained here may be utilized to estimate the elastic modulus $E'$ at temperatures and densities that were not investigated here.

To understand the fatigue resistance of the CNT structures as a function of temperature, the pillars were compressed to 100 cycles at RT and 750 °C. The load-displacement data were converted to stress-strain plots which are shown in Fig. 4a at RT and in Fig. 4b at

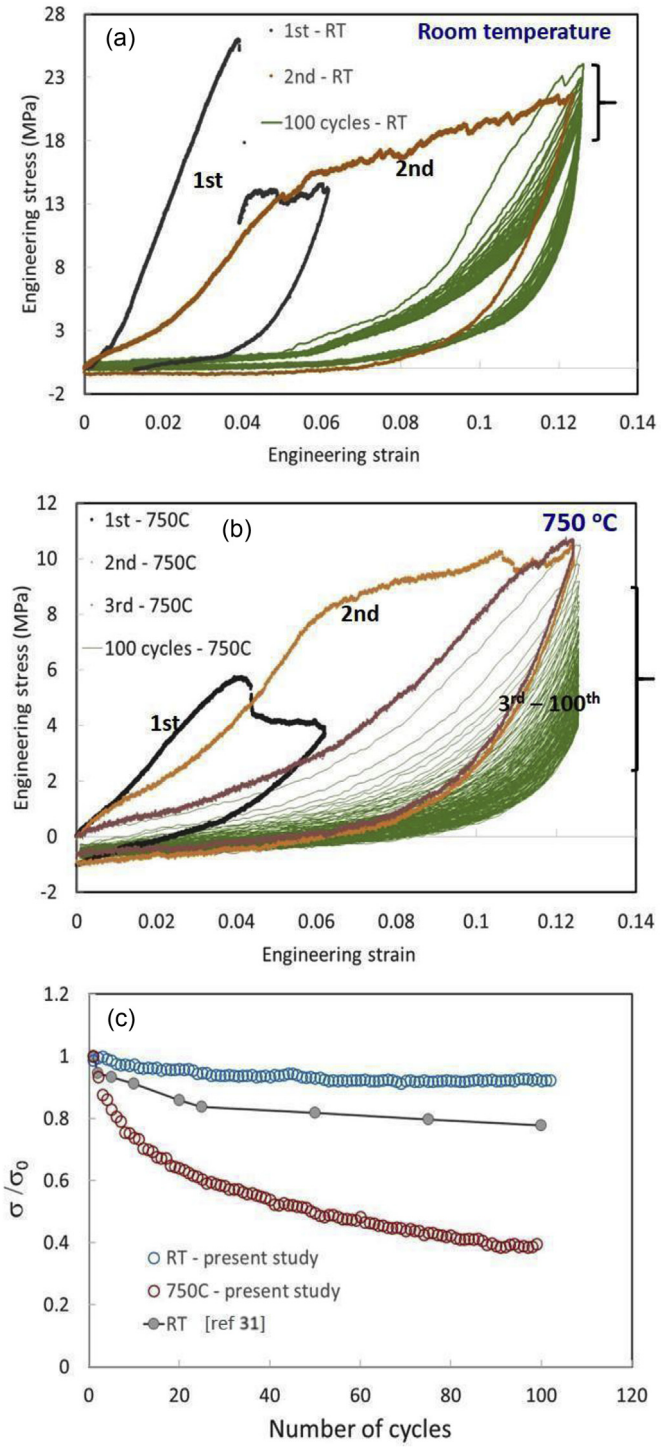


**Fig. 4.** Stress-strain curves of 100 cycles fatigue loading of pillar samples (a) at room temperature, (b) at 750 °C. (c) Plots of compressive stress at 12.5% strain ($\sigma_f$) normalized by compressive stress at 2nd cycle ($\sigma_o$) as a function of number of cycles ($n$). The current data is compared with fatigue loading of a non-interconnected carbon nanotube structure[31]. (A colour version of this figure can be viewed online.)

750 °C. The strain applied in the first cycle (black data) was 6%. The pillar was unloaded and reloaded to 12.5% strain at 2nd cycle (orange data) to 100 cycles (green data). The following features of the deformation process are similar at RT and high temperature. The stress jump, which was present in the first cycle, was absent in the next cycles. In the 2nd cycle, stress-strain curve does not show initial elastic linearity, but shows two distinct regions. The first segment of loading is fairly smooth, and the second segment loading presents many small stress drops. From the 3rd cycle and onward, stress-strain curves show a similar behavior with low stiffness during initial straining and high stiffness during final straining. Although both temperatures showed a similar pattern of deformation, the major difference were the change in compressive flow stress ($\sigma_f$) at the maximum strain. The compressive stress at 12.5% strain, $\sigma_f$, at RT does not change much whereas $\sigma_f$ drops rapidly at 750 °C. To examine the effect of temperature, the maximum compressive stress at 12.5% strain ($\sigma_f$) is normalized with the compressive stress at the 2nd cycle ($\sigma_o$) and plotted in Fig. 4c. The results were also compared with the fatigue study conducted by Ajayan et al. on non-interconnected bonded CNT scaffolds at room temperature [31]. In the current study, $\sigma_f$, 23.9 MPa, at the 2nd cycle gradually drops to 22.3 MPa at 100th cycle (6.69% reduction). Most of the reduction in $\sigma_f$ appears during the initial cycles. The change in $\sigma_f$ was found less than 1% after 30th cycle. At 750 °C, $\sigma_f$ in the 2nd cycle is 10.4 MPa which decreases to 4.1 MPa at 100th cycle (60.57% reduction). The change in $\sigma_f$ in ref 27 at RT is much higher (~20%) than the change observed in the present study which implies that interconnected CNT structures have higher fatigue resistance than non-interconnected structures.

The vertically aligned CNTs (VACNT) and their structures are associated with both covalent and van der Waal bonding in the network [32]. The bonding between the neighboring carbon atoms in an individual CNT are $sp^2$ covalent resulting in superior mechanical properties. However, in most studies on VACNT, individual nanotubes are mainly attached by weak van der Waals force. The reported values of the elastic modulus of such non-interconnected VACNT varies between 30 KPa and 100 MPa as predicted by eq. (1) with low interaction factor values, unless the structure is used as a reinforcement component in composite materials [32]. The average elastic modulus of 640 MPa obtained in this study is the highest reported by any literature for a 3D CNT structure without an embedded matrix and coating. The enhancement of modulus is due to the presence of covalently bonded interconnects. A reduction in porosities can result in higher elastic modulus, however, the density of the structure in this study is not significantly different from other studies [31].

In the fatigue study, characteristic viscoelastic-induced hysteresis with nonlinear loading curve was observed after the 2nd cycle. Two distinct trajectories can be noticed in the stress-strain curves in the loading and unloading segments. The hysteresis loops do not change significantly with cycles at RT showing a steady state, which can be described as shape memory characteristic. This behavior can be compared with the preconditioning nature of such structure described by Ajayan et al. [32]. The fatigue resistance of the structure was measured at a constant compressive strain as a function of cycles. Most of the reduction in maximum compressive stress, $\sigma_f$, happened during initial cycles and only 1% stress dropped occurs after 30 cycles to 100 cycles. As mentioned earlier, the first cycle of the loading caused irreversible buckling deformation at the base of the pillar. The next few cycles made subsequent smaller buckling events reaching a steady state after a few cycles. It could also be noticed that unloading curves did not show any change as loading curve which confirms buckling events are irreversible deformation. Two trajectory behavior in the loading segment can be explained using the concepts applied to other porous and foam materials. The low stiffness part of the curve appears due to reversible bending of the structure, and after certain strain the sharp increase in the stiffness is due to densification of the structure. The fitting of the straight lines at low stiffness region and high stiffness region confirms that the change from one deformation mode to another appears at a critical strain which is 9.7% at 3rd

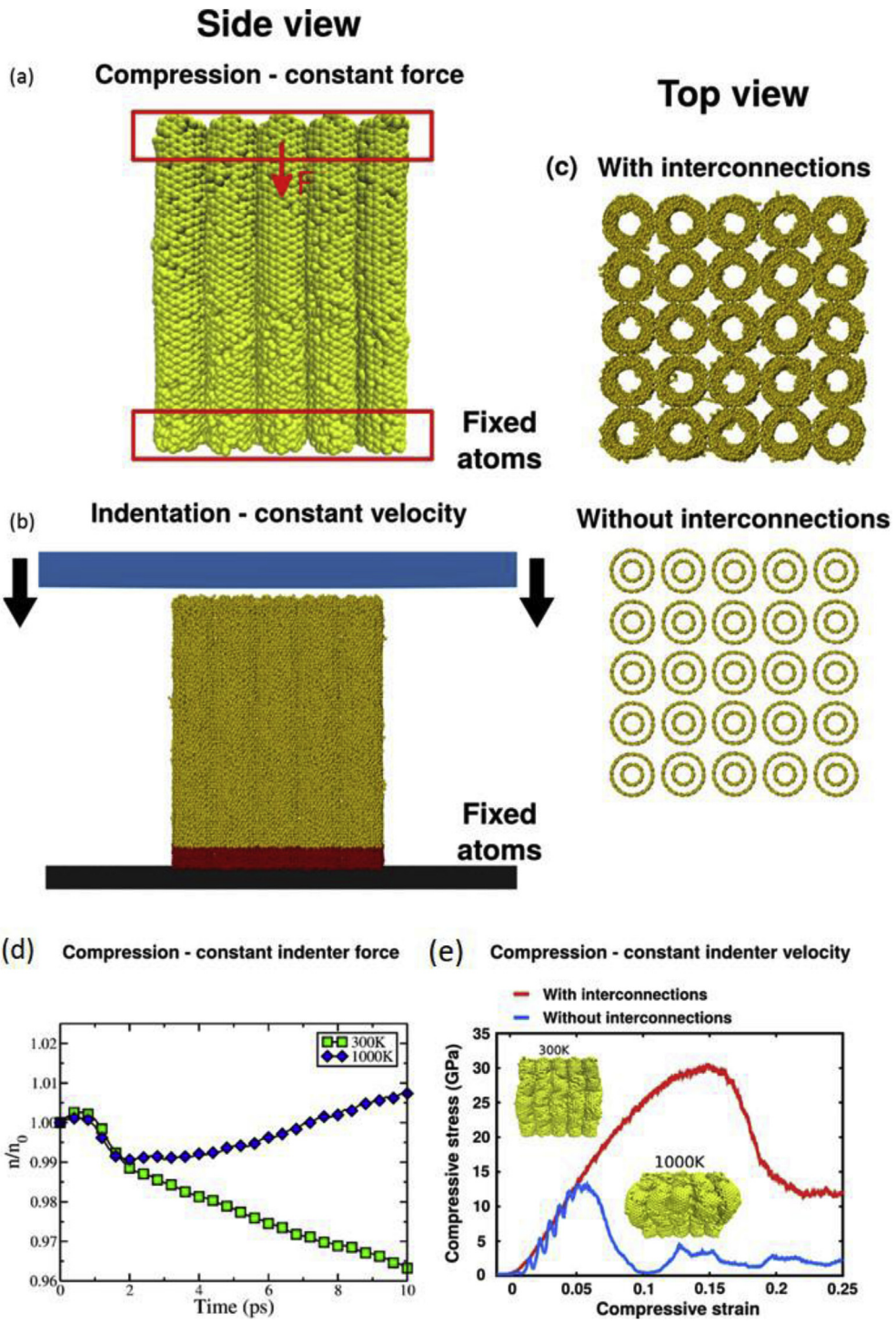


**Fig. 5.** (a) Schematic view of the setup employed in MD simulations to compress a model CNT pillar with a constant force. (b) Schematic view of a setup used in compression tests, where a rigid indenter was displaced downwards at constant velocity, and the response force was recorded. (c) Cross-section of model pillars with and without interconnections. (d) Results from constant force MD simulations. $n$ is the current number of bonds at a particular time, and $n_0$ is the initial number of bonds. Inset showing snapshots taken at $t = 10$ ps for simulations considering two temperatures. (e) Results from CNT pillar compression at constant velocity. Model structures without interconnections support much lower loads, despite being composed of stronger defect-free CNTs. (A colour version of this figure can be viewed online.)

cycle and increases to 11.2% at 100th cycle. The stress-strain curve changes significantly with temperature although the overall nature remains similar. Hysteresis loops decrease considerable when the tests were conducted at 750 °C as shown in Fig. 4b. The critical strain for change in deformation mode appears at 7.8% at 3rd cycle and 13% at 100$^{th}$ cycle.

To better understand the nanoscopic behavior of carbon nanotube pillars under pressure at higher temperatures, we have performed molecular dynamics simulations (MD) on CNT structures at low and high temperatures. In the setup used in these simulations, a constant force was applied to compress model pillars at 27 °C (300 K) and 727 °C (1000 K), Fig. 5. To evaluate how compression

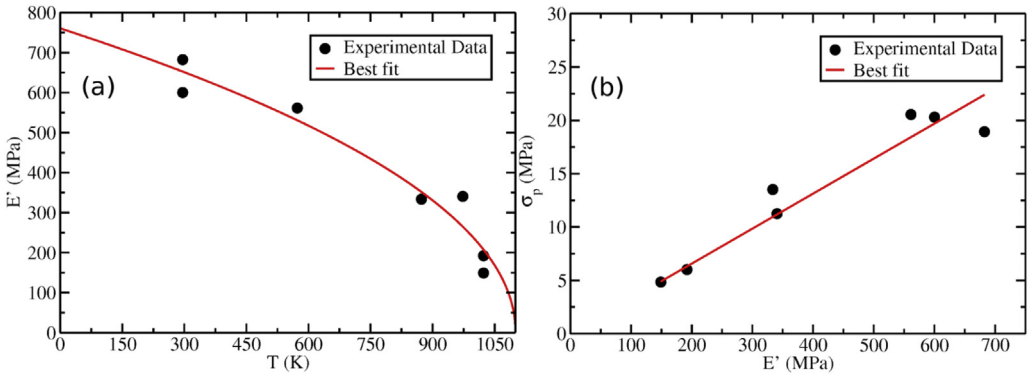


**Fig. 6.** Best fit curves of (a) effective elastic modulus $E^{'}$ as a function of the temperature T showing an accentuated drop and (b) plateau strength $\sigma_p$ as a function of $E^{'}$. (A colour version of this figure can be viewed online.)

modified the structure of CNTs, the total number of bonds in the model structure was tracked over time. At room temperature, compression leads to a decrease in bond number, $n/n_0$. $n$ represents the current number of bonds at a particular time scale and $n_0$ is the initial number of bonds, as shown in Fig. 5d. At a higher temperature (727 °C), after an initial decrease in the number of bonds, $n$ actually increases, due to bond reconstruction. At the simulation end, the number of bonds formed had surpassed the number of broken bonds, as the high temperature and pressure favored bond reconstruction. Such a process may account for the strengthening of the material under compression during the initial cycles. It is important to emphasize that high temperature may favor the formation of atomic bonds, but weaken the underlying networks and also allow increased thermal vibrations in the structure. An MD trajectory of a compressive test at constant force is presented in the supplementary material (Video S1). Observe the structure buckles readily at higher temperature.

Compression MD simulations were also carried out on CNT pillars with and without interconnections to investigate their effect on the mechanical properties. A planar indenter was moved towards the pillar at a constant velocity (see Fig. 5b). The results, displayed in Fig. 5e, show that the maximum stress supported by the structure at a given strain before failure was higher in the presence of interconnections. The major deformation mode was observed to be bending or buckling failure of nanotubes. For the case of non-interconnected structure, as the local stress values increased, nanotubes were free to bend individually. The bending mode decreases the overall stress leading to non-monotonic stress behavior observed in Fig. 5e. The simulation study shows that interconnects play a key role to prevent localized bending at a low strain. The result corroborates our assertion that enhanced mechanical properties found in the experimental part of this study are due to the presence of covalently bonded interconnects. This result might be better visualized with the aid of Video S2 of the supplementary material. Observe that the CNTs in the structure without interconnections readily bend in different directions under compression. Meanwhile, the CNTs in the structure with interconnections remain vertical initially (undergoing compression) and, as strain increases, eventually bend collectively.

## 3. Conclusion

In summary, nanomechanical behavior of chemically interconnected 3D CNT structures without a matrix was investigated using a high-temperature nanomechanical instrument inside an SEM. The covalently bonded structure showed elastic modulus of 640 MPa which is significantly higher than elastic modulus of non-interconnected CNT structures reported in the literature. A strong dependency of temperature on elastic modulus was observed. Elastic modulus decreases linearly with increasing temperature and 70% reduction in elastic modulus was measured at 750 °C. Buckling at the base of the pillar was found as a major mode of permanent deformation at room temperature as well as at elevated temperatures. Critical stress required for first buckling event decreases gradually with increasing temperature whereas net stress change due to first buckle formation drops significantly only at 300 °C. Compression fatigue experiments showed that maximum load bearing stress at a particular strain reduced by a small amount at RT (6.69%) and significantly at 750 °C (60.57%) after 100 cycles of loading. The nature of the cyclic stress-strain curves remains the same at RT and higher temperature. Analytical modelling and MD simulations of compression of pillars revealed that interconnections improve mechanical properties of CNT pillars by preventing localized bending of nanotubes during compression.

## Acknowledgements

S.O. acknowledges financial support from a LANL Director's Postdoctoral Fellowship. LDM, and DSG acknowledge the Brazilian Research Agencies CNPq, CAPES, and FAPESP for financial support. DSG also acknowledges the Center for Computational Engineering and Sciences at Unicamp through the FAPESP/CEPID Grant No. 2013/08293-7, for computational and financial support.

N.M.P. is supported by the European Commission H2020 under the Graphene Flagship Core 2 grant no. 785219 (WP14, Composites) and under the FET Proactive ("Neurofibres" no. 732344), as well as by the Italian Ministry of Education, University and Research (MIUR) under the "Departments of Excellence" grant no. L.232/2016 and by Fondazione Caritro under "Self-Cleaning Glasses" no. 2016.0278. R.A.B. acknowledges financial support from Fondazione Caritro.

## Appendix A. Supplementary data

Supplementary data to this article can be found online at https://doi.org/10.1016/j.carbon.2018.09.075.

## References

[1] H.J. Dai, Carbon Nanotubes: synthesis, integration, and properties, Acc. Chem. Res. 35 (2002) 1035–1044, https://doi.org/10.1021/ar0101640.
[2] S.I. Cha, K.T. Kim, K.H. Lee, C.B. Mo, Y.J. Jeong, S.H. Hong, Mechanical and electrical properties of cross-linked carbon nanotubes, Carbon 46 (2008) 482–488. https://doi.org/10.1016/j.carbon.2007.12.023.
[3] R.H. Baughman, A.A. Zakhidov, W.A. de Heer, Carbon nanotubes - the route toward applications, Science 297 (2002) 787–792, https://doi.org/10.1126/

science.1060928.
[4] L. Ma, A.H.C. Hart, S. Ozden, R. Vajtai, P.M. Ajayan, Spiers memorial lecture advances of carbon nanomaterials, Faraday Discuss 173 (2014) 9–46, https://doi.org/10.1039/C4FD90039A.
[5] S. Ozden, T.N. Narayanan, C.S. Tiwary, P. Dong, A.H.C. Hart, R. Vajtai, P.M. Ajayan, 3D macroporous solids from chemically cross-linked carbon nanotubes, Small 11 (2015) 688–693. https://doi.org/10.1002/smll.201402127.
[6] J.M. Schnorr, T.M. Swager, Emerging applications of carbon nanotubes, Chem. Mater. 23 (2011) 646–657.
[7] S. Ozden, L. Ge, T.N. Narayanan, A.H.C. Hart, H. Yang, S. Sridhar, R. Vajtai, P.M. Ajayan, Anisotropically functionalized carbon nanotube Array based hygroscopic scaffolds, ACS Appl. Mater. Interfaces 6 (2014) 10608–10613, https://doi.org/10.1021/am5022717.
[8] Z.P. Zeng, X.C. Gui, Z.Q. Lin, L.H. Zhang, Y. Jia, A.Y. Cao, Y. Zhu, R. Xiang, T.Z. Wu, Z.K. Tang, Carbon nanotube sponge-array tandem composites with extended energy absorption range, Adv. Mater. 25 (2013) 1185–1191. https://doi.org/10.1002/adma.201203901.
[9] X.C. Gui, J.Q. Wei, K.L. Wang, A.Y. Cao, H.W. Zhu, Y. Jia, Q.K. Shu, D.H. Wu, Carbon nanotube sponges, Adv. Mater. 22 (2010) 617–621. https://doi.org/10.1002/adma.200902986.
[10] C.S. Shan, W.J. Zhao, X.L. Lu, D.J. O'Brien, Y.P. Li, Z.Y. Cao, A.L. Elias, R. Cruz-Silva, M. Terrones, B.Q. Wei, J. Suhr, Three-dimensional nitrogen-doped multiwall carbon nanotube sponges with tunable properties, Nano Lett. 13 (2013) 5514–5520, https://doi.org/10.1021/nl403109g.
[11] R.S. Ruoff, D. Qian, W.K. Liu, Mechanical properties of carbon nanotubes: theoretical predictions and experimental measurements, C. R. Phys. 4 (2003) 993–1008. https://doi.org/10.1016/j.crhy.2003.08.001.
[12] B.J. Carey, P.K. Patra, L. Ci, G.G. Silva, P.M. Ajayan, Observation of dynamic strain hardening in polymer nanocomposites, ACS Nano 5 (2011) 2715–2722, https://doi.org/10.1021/nn103104g.
[13] Y.Y. Shang, X.D. He, Y.B. Li, L.H. Zhang, Z. Li, C.Y. Ji, E.Z. Shi, P.X. Li, K. Zhu, Q.Y. Peng, C. Wang, X.J. Zhang, R.G. Wang, J.Q. Wei, K.L. Wang, H.W. Zhu, D.H. Wu, A.Y. Cao, Super-stretchable spring-like carbon nanotube ropes, Adv. Mater. 24 (2012) 2896–2900. https://doi.org/10.1002/adma.201200576.
[14] L.M. Jonsson, L.M. Jonsson, S. Axelsson, T. Nord, S. Viefers, J.M. Kinaret, High frequency properties of a CNT-based nanorelay, Nanotechnology 15 (2004) 1497–1502, https://doi.org/10.1088/0957-4484/15/11/022.
[15] S. Pathak, E.J. Lim, P.S.S. Abadi, S. Graham, B.A. Cola, J.R. Greer, Higher recovery and better energy dissipation at faster strain rates in carbon nanotube bundles: an in-situ study, ACS Nano 6 (2012) 2189–2197, https://doi.org/10.1021/nn300376j.
[16] S.B. Hutchens, L.J. Hall, J.R. Greer, In situ mechanical testing reveals periodic buckle nucleation and propagation in carbon nanotube bundles, Adv. Funct. Mater. 20 (2010) 2338–2346. https://doi.org/10.1002/adfm.201000305.
[17] S. Vinod, C.S. Tiwary, L.D. Machado, S.O. Ozden, R. Vajtai, D.S. Galvao, P.M. Ajayan, Synthesis of ultralow density 3D graphene-CNT foams using a two-step method, Nanoscale 8 (2016) 15857–15863, https://doi.org/10.1039/C6NR04252J.
[18] A.E. Aliev, J.Y. Oh, M.E. Kozlov, A.A. Kuznetsov, S.L. Fang, A.F. Fonseca, R. Ovalle, M.D. Lima, M.H. Haque, Y.N. Gartstein, M. Zhang, A.A. Zakhidov, R.H. Baughman, Giant-stroke, superelastic carbon nanotube Aerogel muscles, Science 323 (2009) 1575–1578, https://doi.org/10.1126/science.1168312.
[19] S. Ozden, C.S. Tiwary, A.H.C. Hart, A.C. Chipara, R. Romero-Aburto, M.T.F. Rodrigues, J. Taha-Tijerina, R. Vajtai, P.M. Ajayan, Density variant carbon nanotube interconnected solids, Adv. Mater. 27 (2015) 1842–1850. https://doi.org/10.1002/adma.201404995.
[20] S. Ozden, Y. Yang, C.S. Tiwary, S. Bhowmick, S. Asif, E.S. Penev, B.I. Yakobson, P.M. Ajayan, Indentation tests reveal geometry-regulated stiffening of nanotube junctions, Nano Lett. 16 (2016) 232–236, https://doi.org/10.1021/acs.nanolett.5b03607.
[21] J.E. Mueller, A.C.T. van Duin, W.A. Goddard, Development and validation of ReaxFF reactive force field for hydrocarbon chemistry catalyzed by nickel, J. Phys. Chem. C 114 (2010) 4939–4949, https://doi.org/10.1021/jp9035056.
[22] A.C.T. Van Duin, S. Dasgupta, F. Lorant, W.A. Goddard, W.A. ReaxFF, A reactive force field for hydrocarbons, J. Phys. Chem. 105 (2001) 9396–9409, https://doi.org/10.1021/jp004368u.
[23] S. Plimpton, Fast parallel algorithms for short-range molecular-dynamics, J. Comput. Phys. 117 (1995) 1–19. https://doi.org/10.1006/jcph.1995.1039.
[24] M.S. Dresselhaus, G. Dresselhaus, R. Saito, A. Jorio, Raman spectroscopy of carbon nanotubes, Phys. Rep. 409 (2005) 47–99. https://doi.org/10.1016/j.physrep.2004.10.006.
[25] A.A. Zbib, S.D. Mesarovic, E.T. Lilleodden, D. McClain, J. Jiao, D.F. Bahr, The coordinated buckling of carbon nanotube turfs under uniform compression, Nanotechnology 19 (2008), https://doi.org/10.1088/0957-4484/19/17/175704.
[26] A.Q. Qiu, D.F. Bahr, The role of density in the mechanical response of CNT turfs, Carbon 55 (2013) 335–342. https://doi.org/10.1016/j.carbon.2012.12.073.
[27] C.Q. Sun, H.L. Bai, B.K. Tay, S. Li, E.Y. Jiang, Dimension, strength, and chemical and thermal stability of a single C–C bond in carbon nanotubes, J. Phys. Chem. B 107 (31) (2003) 7544–7546, https://doi.org/10.1021/jp035070h.
[28] T. Dumitrica, M. Hua, B. I. Yakobson, Symmetry-, time-, and temperature-dependent strength of carbon nanotubes. Proc. Natl. Acad. Sci. Unit. States Am. 103 (16) 6105-6610, https://doi.org/10.1073/pnas.0600945103.
[29] M. Pavese, S. Musso, N.M. Pugno, Compression behaviour of thick vertically aligned carbon nanotube blocks, J. Nanosci. Nanotechnol. 10 (2010) 4240–4245, https://doi.org/10.1166/jnn.2010.2187.
[30] H. Qi, et al., Determination of mechanical properties of carbon nanotubes and vertically aligned carbon nanotube forests using nanoindentation, J. Mech. Phys. Solid. 51 (11) (2003) 2213–2237, https://doi.org/10.1016/j.jmps.2003.09.015.
[31] J. Suhr, P. Victor, L.C.S. Sreekala, X. Zhang, O. Nalamasu, P.M. Ajayan, Fatigue resistance of aligned carbon nanotube Arrays under cyclic compression, Nat. Nanotechnol. 2 (2007) 417–421, https://doi.org/10.1038/nnano.2007.186.
[32] Y. Zeng, L. Ci, J.B. Carey, R. Vajtai, P.M. Ajayan, Design and reinforcement: vertically aligned carbon nanotube-based sandwich composites, ACS Nano 4 (2010) 6798–6804, https://doi.org/10.1021/nn101650p.

Supporting Information

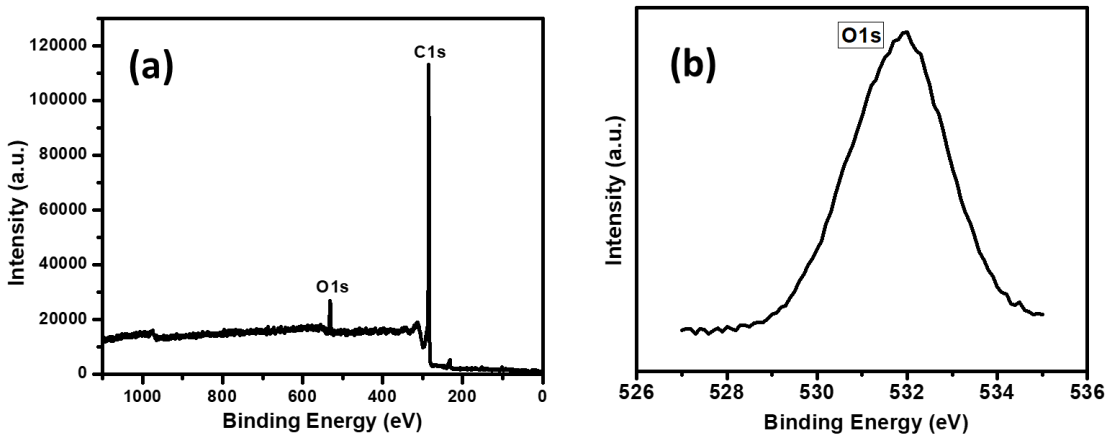


Figure S1. (a) The survey XPS spectra of CNTs, (b) elemental scan of Oxygen.

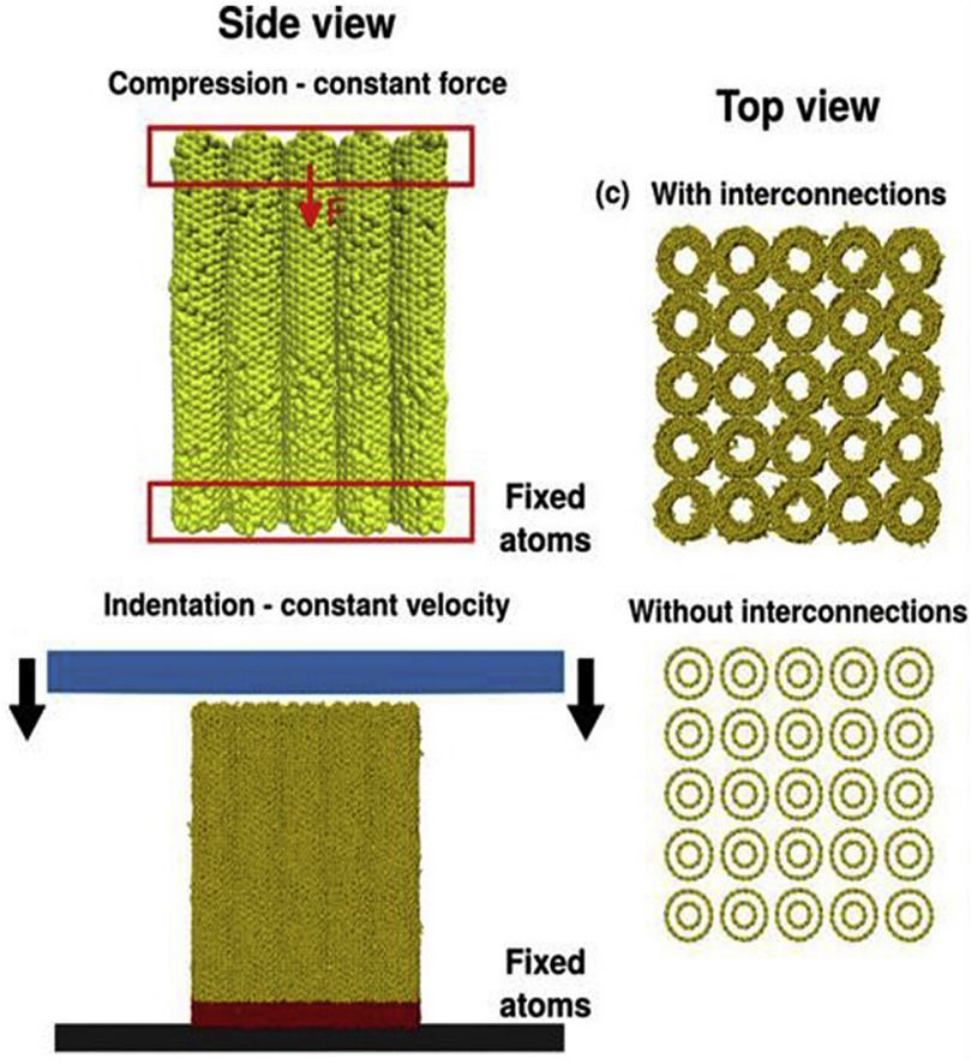
Side view
Compression - constant force
F
Fixed atoms
Indentation - constant velocity
Fixed atoms
Top view
(c) With interconnections
Without interconnections

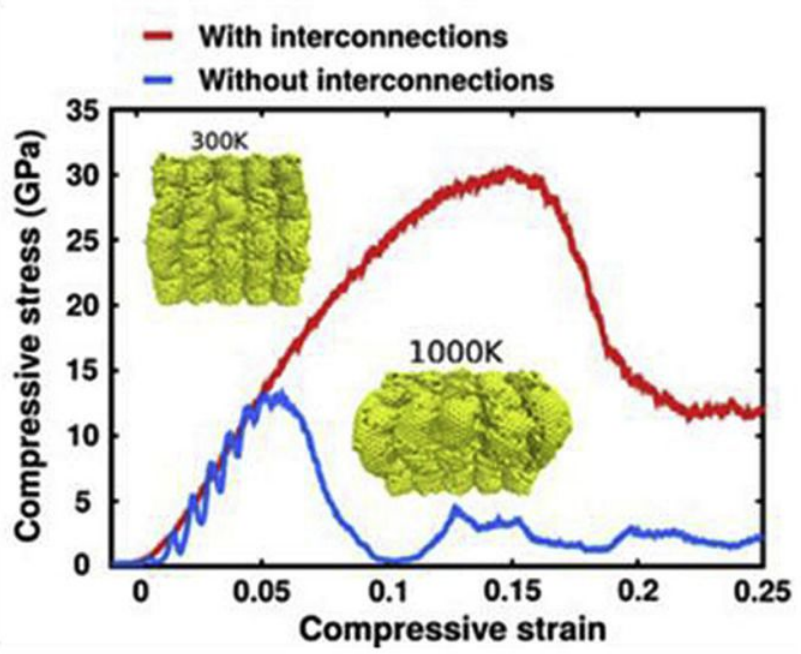
With interconnections
Without interconnections
300K
1000K
Compressive stress (GPa)
Compressive strain
0
5
10
15
20
25
30
35
0
0.05
0.1
0.15
0.2
0.25